

PAPER

Equilibrium shape of misfitting precipitates with anisotropic elasticity and anisotropic interfacial energy

To cite this article: Tushar Joshi *et al* 2020 *Modelling Simul. Mater. Sci. Eng.* **28** 075009

View the [article online](#) for updates and enhancements.

You may also like

- [Origin of magnetization-induced anisotropy of magnetic films](#)
Jin Han-Min, Chong-Oh Kim, Taek-Dong Lee *et al.*
- [Estimation of optical absorption in anisotropic background](#)
Jenni Heino and Erkki Somersalo
- [\(Invited\) Anisotropic Self-Oscillating Reaction in Liquid Crystalline Nanosheets Hydrogels](#)
Nobuyoshih Miyamoto, Morio Shintate, Takumi Inadomi *et al.*



IOP | ebooks™

Bringing together innovative digital publishing with leading authors from the global scientific community.

Start exploring the collection—download the first chapter of every title for free.

Equilibrium shape of misfitting precipitates with anisotropic elasticity and anisotropic interfacial energy

Tushar Joshi¹, Rajat Arora², Anup Basak³ and Anurag Gupta^{1,4} 

¹ Mechanical Engineering, Indian Institute of Technology Kanpur, UP, 208016, India

² Ansys, Inc., Canonsburg, PA, 15317, United States of America

³ Mechanical Engineering, Indian Institute of Technology Tirupati, AP, 517506, India

E-mail: ag@iitk.ac.in

Received 4 June 2020, revised 27 July 2020

Accepted for publication 11 August 2020

Published 22 September 2020



CrossMark

Abstract

Extended finite element method and anisotropic level set method are coupled to determine locally stable equilibrium shapes of homogeneous and inhomogeneous precipitates in a large matrix. The bulk elasticity and the interfacial energy density are both allowed to be anisotropic while the misfit strain is kept dilatational. The anisotropy in the crystalline interfacial energies, incorporated through a dependence on the orientation, renders the evolution equation unstable for certain orientation regimes. The equation is regularized by adding a curvature term in the interface energy density which in turn requires the level set method to be modified suitably. The developed methodology is verified for several existing solutions before obtaining new results in the presence of anisotropic interfacial energy. Equilibrium shapes are obtained both for single and multiple precipitates with an emphasis on the interplay between the anisotropies in bulk elasticity and interface energy density.

Keywords: equilibrium shape of precipitate, level set method, extended finite element method, anisotropic crystalline energies

(Some figures may appear in colour only in the online journal)

1. Introduction

The two-dimensional shape optimization problem, which seeks to determine the equilibrium shape of multiple precipitates, with fixed total area, under various geometric and material

⁴ Author to whom any correspondence should be addressed.

assumptions has been discussed actively in the literature [12, 16, 22, 23, 27, 29, 31, 32]. There are several factors which influence the solution of the problem: isotropic or anisotropic bulk elasticity, isotropic (constant) or anisotropic (orientation dependent) interfacial energy density, interface elasticity, precipitates as inhomogeneities (material properties in the precipitate different from that of matrix), single or multiple precipitates, nature of misfit strain in the precipitates, size of the precipitates, and location of the precipitate with respect to the boundary of the domain. The increasing complexity of the problem has required increased sophistication in the solution methodology. The numerical methods have been based either on a boundary integral formulation [15, 16, 22, 23] or a finite element based technique [11, 32], assuming sharp interfaces, or phase-field methods [3, 31] which assume diffusive interfaces. The present work revisits the problem for single and multiple precipitates (in a large matrix), possibly inhomogeneous, with dilatational misfit strains, and anisotropies in both bulk elasticity and interfacial energy density. We assume the precipitate-matrix interface to be sharp. Our solution procedure is based on a novel formulation which couples extended finite element method (XFEM) with anisotropic level set method (LSM).

The simplest case of a single precipitate in a large matrix, with different material properties and dilatational misfit strain, considering isotropy in both bulk elasticity and interface energy density was discussed analytically by Johnson and Cahn [12]. Their work was extended to include anisotropic (cubic) bulk elasticity and tetragonal misfit strains, although with a precipitate having identical material properties as the bulk, by Thompson *et al* [29] for an isolated precipitate and Su and Voorhees [27, 28] for multiple precipitates. The inhomogeneous precipitates were discussed in detail by Gross *et al* [15, 22, 23]. The anisotropy in interfacial energy, and orthotropy in bulk elasticity, were incorporated by Leo *et al* [16] using a boundary integral method. Interfacial elasticity was considered by Zhao *et al* [32], while ignoring anisotropy in the interface energy, within a computational framework which coupled XFEM and isotropic LSM. In parallel with the above development, which was in the context of sharp interfaces, the problem was also studied using phase-field methods [31]; we note, in particular, the recent work by Bhadak *et al* [3] which included some results on equilibrium shape of single precipitates with anisotropic interfacial energy.

On one hand, our work can be seen as an extension of the solution approach introduced by Zhao *et al* [32] by incorporating anisotropic energies in the LSM. The anisotropy of the crystalline surface energies is such that it renders the governing evolution equation backward-parabolic, for certain orientations, and hence unstable [5]. The equation is regularized by appending a dependence on curvature in the interface energy density, although at the cost of increased numerical complexity. In this work we adapt the anisotropic level set formulation developed by Basak and Gupta [1], previously in the context of grain boundary motion, and couple it with the XFEM of Moës *et al* [18]. On the other hand, our methodology provides an alternative treatment to the fully anisotropic problem of determining the equilibrium shape vis-à-vis the boundary integral method of Leo *et al* [16]. In comparison, our framework can deal seamlessly with topological changes in the precipitate shape evolution, as well as merger and splitting, thereby exploring wider possible configurations for the sought equilibrium shape. It is better equipped for handling the evolution of curves having regions of high curvature, and also for investigating the problems with finite (or semi-finite) domains where the precipitates are located close to a boundary.

After presenting the theoretical aspects of the formulation in section 2, we outline our numerical strategy in section 3. The latter involves coupling of XFEM and anisotropic LSM. The development of this coupled framework, involving an anisotropic interfacial energy, is the central contribution of this work. Subsequently, we present the results of our simulations in section 4. Most of our results with isotropic interfacial energy have appeared previously and

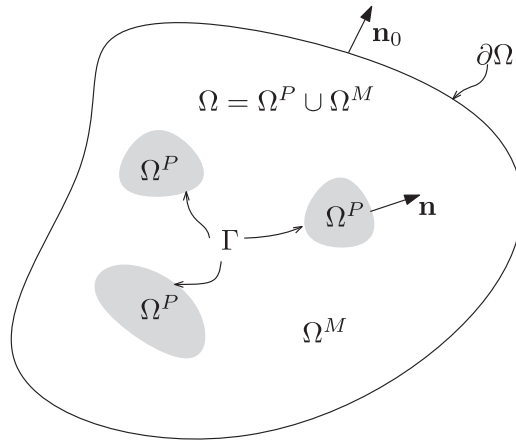


Figure 1. The problem domain Ω .

are used here as verifications of our numerical strategy. The results with anisotropic interfacial energy provide several novel insights into an old problem. Our emphasis therein is to understand the interplay between anisotropies in bulk elasticity and interfacial energy leading to different equilibrium shapes of a precipitate at different parametric values. We conclude the paper in section 5.

2. Problem formulation

We consider a two-dimensional (2D) domain Ω , with a regular boundary $\partial\Omega$, containing several precipitates, with arbitrary shapes having regular boundaries, see figure 1. The combined domain occupied by the precipitates is denoted as Ω^P whereas the matrix domain is denoted as Ω^M such that $\Omega^P \cup \Omega^M = \Omega$ and $\Omega^P \cap \Omega^M = \emptyset$. The precipitate domain Ω^P is assumed to carry a constant misfit strain ϵ^* . We use Γ to represent the union of all interfaces between the matrix and the precipitate domain, \mathbf{n} for the unit outward normal to Γ (pointing into the matrix), and \mathbf{n}_0 for the unit outward normal to $\partial\Omega$. The linearized strain ϵ is related to the displacement vector field \mathbf{u} in the usual way, $\epsilon = (1/2)(\nabla\mathbf{u} + (\nabla\mathbf{u})^T)$, away from Γ , where ∇ is the gradient operator with respect to the position field $\mathbf{x} \in \Omega$ and superscript T denotes the transpose. Across Γ , we assume \mathbf{u} to remain continuous (but not necessarily differentiable), i.e., $[[\mathbf{u}]] = \mathbf{0}$, where the bracket represents a jump in the enclosed field across Γ . The displacement field is otherwise assumed to be smooth in Ω away from Γ . The strain field is therefore piecewise smooth in Ω but possibly discontinuous across Γ .

The piecewise smooth Cauchy stress tensor σ , in the absence of body forces and inertia, satisfies the equilibrium conditions

$$\operatorname{div} \sigma = \mathbf{0} \quad \text{in } \Omega/\Gamma, \quad \sigma \mathbf{n}_0 = \mathbf{0} \quad \text{on } \partial\Omega, \quad \text{and} \quad [[\sigma]] \mathbf{n} = \mathbf{0} \quad \text{on } \Gamma, \quad (1)$$

where div is the divergence operator. The second equation above denotes the traction-free boundary condition while the third condition enforces traction continuity across the interfaces. Assuming the constitutive behavior of the domain to be linear elastic, we can relate the stress

tensor to the strain tensor as

$$\boldsymbol{\sigma}(\mathbf{x}) = \mathbb{C}\boldsymbol{\epsilon}(\mathbf{x}) = \begin{cases} \mathbb{C}^P(\boldsymbol{\epsilon}(\mathbf{x}) - \boldsymbol{\epsilon}^*), & \text{if } \mathbf{x} \in \Omega^P, \text{ and} \\ \mathbb{C}^M\boldsymbol{\epsilon}(\mathbf{x}), & \text{if } \mathbf{x} \in \Omega^M, \end{cases} \quad (2)$$

where $\boldsymbol{\epsilon}$ is the elastic strain tensor (equal to $\boldsymbol{\epsilon} - \boldsymbol{\epsilon}^*$ in Ω^P and $\boldsymbol{\epsilon}$ in Ω^M); \mathbb{C}^P and \mathbb{C}^M are the fourth-order elastic stiffness tensors in the precipitate and the matrix domain, respectively. For a given misfit strain $\boldsymbol{\epsilon}^*$ and precipitate shape Γ , the preceding considerations are sufficient to determine the unique stress field in Ω . The precipitate shape however may not be the equilibrium shape in the sense that it does not lead to a (locally) minimum energy configuration. In order to achieve the equilibrium shape, we allow the interface Γ to evolve, while keeping the precipitate area fixed, until a minimum in total energy is achieved. The kinetics governing the interfacial evolution is discussed next.

The equilibrium shape of the precipitates minimize the total energy of the system while maintaining a constant net area occupied by the precipitates. The energy functional, to be minimized, is expressed as the sum of the bulk elastic energy stored in Ω/Γ , the interfacial energy associated with Γ , and an energetic cost due to any deviation from the area constraint:

$$E = \int_{\Omega} W dA + \int_{\Gamma} \gamma dl + \lambda \left(\int_{\Omega^P} dA - A_0 \right), \quad (3)$$

where dA and dl are infinitesimal area and line elements, respectively; $W = (1/2)\boldsymbol{\sigma} \cdot \boldsymbol{\epsilon}$, where ‘ \cdot ’ denotes an inner-product, is the elastic strain energy density,

$$\gamma(\phi, \kappa) = \gamma_c(\phi) + \frac{1}{2}\delta_r\kappa^2, \quad \text{with } \gamma_c(\phi) = \gamma_0(1 - \alpha_e \cos(n\phi)), \quad (4)$$

is the anisotropic interfacial energy density, λ is the Lagrange multiplier, and A_0 is the fixed total area of the precipitates. In equation (4), ϕ is the inclination angle of \mathbf{n} with respect to the horizontal axis, κ is the curvature of the interface curve, and $\delta_r \ll 1$ is a regularization parameter [5]; γ_0 , $\alpha_e < 1$, and n are constants (n defines the degree of anisotropy). An isotropic interfacial energy density corresponds to γ being a constant with $\delta_r = 0$. The polar plots of the anisotropic interfacial energy for various n are given in figure 2. Under isothermal conditions, the mechanical version of the second law of thermodynamics requires the net mechanical power spent on Ω to be never less than the change in the total energy of Ω . The former is zero since there are no external forces acting on Ω . Consequently, we require $dE/dt \leq 0$ (t denotes time) which, on using equations (3) and (4), yields $\int_{\Gamma} fVdl \geq 0$, where

$$f = \mathbf{n} \cdot [\mathbf{P}]\mathbf{n} + (\gamma_c + \gamma_c'')\kappa - \delta_r \left(\Delta^s \kappa + \frac{1}{2}\kappa^3 \right) - \lambda \quad (5)$$

is the driving force for interface migration and V is the normal speed of the interface; $\mathbf{P} = W\mathbf{1} - (\nabla\mathbf{u})^T\boldsymbol{\sigma}$ is the Eshelby tensor ($\mathbf{1}$ is the identity tensor), the superscript prime is the derivative with respect to ϕ , and Δ^s is the surface Laplacian (in particular, if s is an arc-length parametrization of the interface then $\Delta^s \kappa = \partial^2 \kappa / \partial s^2$). The derivation of the expression for driving force in equation (5) is available elsewhere [8]. The dissipation inequality is identically satisfied if we assume a linear kinetic law of the form $V = f$, with mobility taken to be identity. The inequality also implies that the migration of the interface leads to a reduction of total energy and henceforth towards a locally minimum position in the energy landscape. The

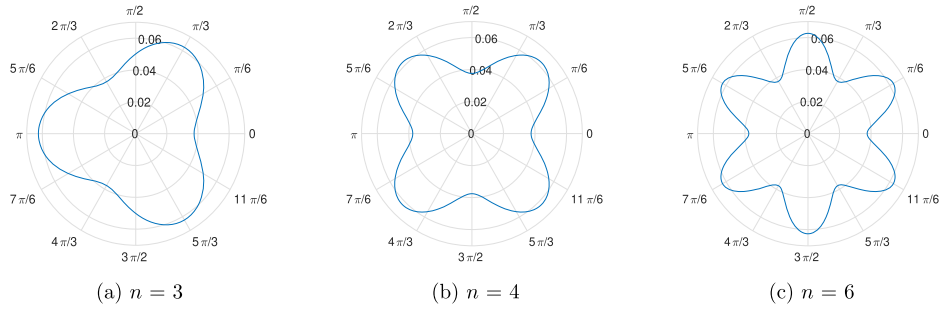


Figure 2. Polar plots for $\gamma_c(\phi) = \gamma_0(1 - \alpha_e \cos(n\phi))$ with $\gamma_0 = 0.05 \text{ J m}^{-2}$ and $\alpha_e = 0.25$.

multiplier λ can be computed using the area conservation condition, $(d/dt) \int_{\Omega^P} dA = 0$, which is equivalent to $\int_{\Gamma} V dl = 0$ or, using the kinetic law, to $\int_{\Gamma} f dl = 0$. We obtain

$$\lambda = \frac{\int_{\Gamma} \left(\mathbf{n} \cdot \llbracket \mathbf{P} \rrbracket \mathbf{n} + (\gamma_c + \gamma_c'')\kappa - \delta_r \left(\Delta^s \kappa + \frac{1}{2} \kappa^3 \right) \right) dl}{\int_{\Gamma} dl}. \quad (6)$$

The interfacial normal speed is now expressed completely in terms of bulk deformation, energy densities, and precipitate geometry. A similar kinetic framework, with γ constant, was used in the works of Schmidt and Gross [22] and Zhao *et al* [32].

3. Methodology for numerical solutions

To simulate the evolution of precipitate boundary and obtain the equilibrium shape, we use a numerical scheme which couples XFEM with LSM. The former solves for the state of stress in the domain, for fixed precipitate shapes, while the latter method is used to evolve the interfaces to new positions, and hence to obtain updated precipitate shapes, for a known value of stress field in the domain. The shape of the interface is represented implicitly as the zero level set of a smooth function $\psi(\mathbf{x}, t)$ over Ω . The evolution of this function is governed by the Hamilton–Jacobi equation in terms of the normal velocity V of the interface. The velocity is given, through the linear kinetic relation, in terms of the geometry of the interface, constitutive parameters, and the bulk stress field. A single level set function is sufficient to take care of complex topological changes such as merging or splitting of precipitates. The bulk fields enter the expression for V only through the normal projection of the jump in Eshelby tensor \mathbf{P} across Γ . The bulk fields are calculated using XFEM. The standard FEM requires re-meshing at every time step to conform with the evolving interface, so as to maintain accuracy and optimal convergence. The XFEM avoids these complications by using the same mesh for the entire simulation process at the cost of nodal enrichment in the neighborhood of the interface. We follow Moës *et al* [18] and Belytschko *et al* [2] to write the XFEM code as required for this work. Our strategy to couple XFEM and LSM is motivated from Duddu *et al* [6]. A brief summary of the XFEM framework is given in section 3.1 below. The details of our XFEM implementation, as well as the XFEM–LSM coupling, and its verification against existing solutions can be found in a recent thesis work [13].

The anisotropic LSM used in this work was developed by Basak and Gupta [1] following the local LSM of Peng *et al* [20]. The local LSM, which is a modification of the classical LSM [19,

24], incorporates the discretization and the reinitialization schemes proposed by Jiang and Peng [10], Russo and Smereka [21], and Smereka [26]. The Hamilton–Jacobi evolution equation for the level set function can become backward parabolic leading to unstable solutions. The source of this problem is the non-convexity of anisotropic interface energies introduced in equation (4). As a remedy, a quadratic dependence on the curvature κ is appended to the energy [5]. The curvature regularization, however, due to the presence of the second-order gradient of κ , increases the order of the differential equation to four. The higher order derivatives are extremely sensitive to errors in κ during numerical computations; we resolve this by computing $\Delta^s \kappa$ in the manner proposed by Smereka [26]. We summarize our anisotropic LSM in section 3.2 below, while referring the interested reader to our earlier paper [1] for further details.

3.1. The extended finite element method

The extended finite element method, as developed by Moës *et al* [18] (see, Belytschko *et al* [2]), enriches the standard polynomial basis functions in order to capture the non-smooth solution fields such that the underlying mesh remains independent of the morphological evolution of the interface. This (extrinsic) enrichment is done locally by selecting a few enriched nodes close to the discontinuity using the partition of unity (PU) concept. The PU is constructed using the standard finite element shape functions. Due to local enrichment, the element can be classified as standard, when none of the nodes are enriched, when all of the nodes are enriched, or blending, when some of the nodes are enriched.

The displacement vector field is approximated in an element as

$$\mathbf{u}_e = \sum_{i \in I^{\text{std}}} N_i(\mathbf{x}) \mathbf{q}_i + \sum_{i \in I^*} N_i(\mathbf{x}) \zeta(\mathbf{x}) \mathbf{a}_i, \quad (7)$$

where I^{std} is the set of all standard finite element nodes of the element, $I^* \subset I$ is the set of enriched nodes of the element (I is the set of all nodes), ζ is the enrichment function (defined below), $N_i(\mathbf{x})$ are the standard FEM shape functions, and \mathbf{q} and \mathbf{a} are the standard and enriched nodal degree of freedom vectors for the element, respectively. The approximated displacement field in equation (7) can be used to construct an approximate strain field in the element, which can then be used to derive an expression for the element stiffness matrix. The element force vector field can be formulated in terms of the displacement approximation; its appearance is solely due to the presence of misfit strain (in the absence of external forces). The level set function ψ , from the LSM routine, is used to identify the enriched nodes and develop the local enrichment function ζ . An element is added to the set T of enriched elements if there exist two nodes (say i and j) in the element such that $\psi_i \psi_j < 0$, where ψ_i is the value of ψ at the i th node; see figure 3(a) for an illustration. All the nodes identified from set T become part of I^* . Such nodes are assigned additional degrees of freedom. For instance, for a bilinear quadrilateral element intersected by a weak discontinuity, sixteen degrees of freedom are assigned, eight classical and eight enriched. We use an enrichment function, given by Moës *et al* [17], which is non-zero only in the enriched elements:

$$\zeta(\mathbf{x}) = \sum_{i \in I} |\psi_i| N_i(\mathbf{x}) - \left| \sum_{i \in I^*} \psi_i N_i(\mathbf{x}) \right|. \quad (8)$$

The numerical integration involved in the evaluation of element stiffness and element force vector demands different treatment in the standard and the enriched elements. The integration

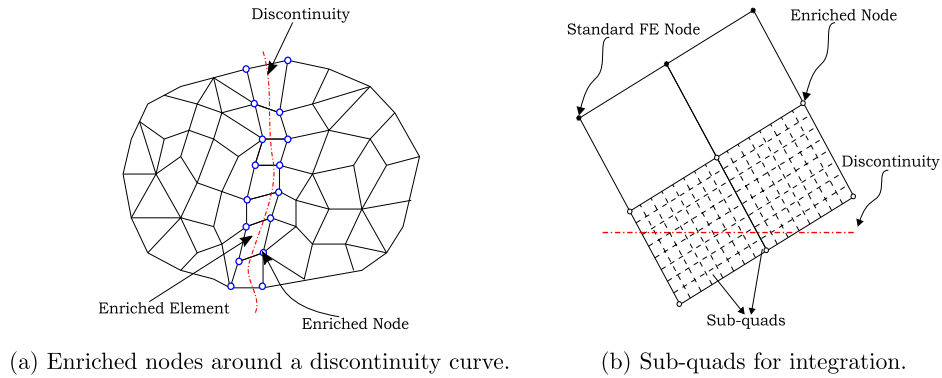


Figure 3. Considerations in the XFEM mesh.

in both standard and blending elements is performed using the Gauss quadrature integral rule for polynomials. For the enriched elements, we divide the element into a number of small sub-quads, e.g., figure 3(b). All the sub-quads, except for those divided by the discontinuity, have consistent properties. The sub-quads, which intersect the discontinuity, can be made consistent on the basis of the area ratio in which the interface cuts the element. The integration is done individually in each of these sub-quads using the simple trapezoidal rule. The accuracy of the integration is controlled by adjusting the number of sub-quads in both the directions. This is verified by performing the integration for some standard functions.

As a result of using enrichment functions, the stiffness matrices in XFEM can become ill-conditioned leading to the failure of using direct methods for solving a linear system of equations. Keeping this in mind, we use the bi-conjugate gradient stabilized method, abbreviated as Bi-CGSTAB, an iterative method for the numerical solution of asymmetric/symmetric linear systems [30]. It is a Krylov subspace method with faster and smoother convergence than bi-conjugate gradient method and conjugate gradient squared method. The accuracy of the numerical solution obtained by Bi-CGSTAB can be optimized by adjusting the solution tolerance.

The steps followed in the XFEM routine can be summarized as follows:

- (a) Generate the mesh for XFEM analysis; the mesh and number of elements will remain unchanged for the entire analysis. We use bilinear quadrilateral elements with a coarse mesh away from the precipitate regions and fine otherwise. The domain size is chosen to be large enough to ignore the boundary effects in order to simulate precipitate evolution in an infinite matrix.
- (b) Use the zero level set of the function ψ , resolved in the LSM routine, to introduce interfaces in the XFEM mesh. Identify the enriched nodes in the mesh.
- (c) Generate the stiffness and the load matrix with suitable integration techniques. The number of sub-quads in the enriched elements is taken as 400 (20×20).
- (d) Solve the system of linear equations using Bi-CGSTAB solver.
- (e) Evaluate the jump in normal projection of the Eshelby tensor across the interface, to be used in the LSM. This is done using the modified domain integral method of Ji and Dolbow [9]. We avoid a direct evaluation of the jump, as a difference of values across the interface, since it can lead to large oscillations in the velocity calculation and affect the convergence of the solution.

3.2. The level set method

The interface Γ between the precipitates and the matrix is considered as the zero level curve of a smooth function $\psi(\mathbf{x}, t)$, where ψ is initialized as a signed distance function (SDF) with ψ negative in the matrix domain Ω^M and positive inside the precipitate domain Ω^P . In the classical LSM, for a given V , ψ is updated with respect to time in the entire domain Ω using the Hamilton–Jacobi equation [24]

$$\frac{\partial \psi}{\partial t} + V \|\nabla \psi\| = 0, \quad (9)$$

where $\|\cdot\|$ denotes the Euclidean norm of a vector. The updated zero level set of ψ gives the new position of the interface Γ . A computationally less expensive local level set scheme has been proposed by Peng *et al* [20], where ψ is updated only in a small domain in the neighborhood of the zero level curve. This is done using the modified Hamilton–Jacobi equation

$$\frac{\partial \psi}{\partial t} + c(\psi)V_{\text{ext}}\|\nabla \psi\| = 0, \quad (10)$$

where $c(\psi)$, a cut-off function, ensures that ψ is updated only in a narrow region surrounding $\psi = 0$, and V_{ext} is the extended normal velocity [1]. The extension q_{ext} of a given field q is determined by solving the hyperbolic equation $(\partial q / \partial t) + (\text{sign } q)(\mathbf{n} \cdot \nabla q) = 0$. The steady state solution of this equation is denoted by q_{ext} ; it satisfies $q_{\text{ext}} = q$ on Γ and remains constant in the direction of the normal to Γ . The updated ψ , obtained from equation (10), in general, does not remain an SDF. This is resolved by reinitializing ψ to an SDF by solving $(\partial d / \partial t) + (\text{sign } d)(\|\nabla d\| - 1) = 0$, such that $d_i = d(\mathbf{x}, 0) = \psi(\mathbf{x}, t)$ [20].

We discretized the square domain Ω using uniform square grids with a mesh size h . Let (x_i, y_j) be the (i, j) th node in the 2D lattice grid. At time step t_n and at the (i, j) th grid point, we denote the level set function by $\psi_{i,j}$. The semi-discrete form of equation (10), using the method of lines, can be written in a form

$$\frac{d\psi_{i,j}}{dt} = \mathcal{L}(\mathbf{x}, \psi_{x,i,j}^{\pm}, \psi_{y,i,j}^{\pm}, \kappa_{i,j}, \mathbf{n}_{i,j}), \quad (11)$$

with $\mathcal{L} = -cV_{\text{ext}}\|\nabla \psi\|$ such that

$$\mathcal{L}_{i,j} = -\max((cV_{\text{ext}})_{i,j}, 0)\|\nabla^+ \psi\|_{i,j} - \min((cV_{\text{ext}})_{i,j}, 0)\|\nabla^- \psi\|_{i,j}, \quad (12)$$

where $\|\nabla^{\pm} \psi\|_{i,j} = [\max(\psi_{x,i,j}^{\mp}, 0)^2 + \min(\psi_{x,i,j}^{\pm}, 0)^2 + \max(\psi_{y,i,j}^{\mp}, 0)^2 + \min(\psi_{y,i,j}^{\pm}, 0)^2]^{1/2}$. Here $\psi_{x,i,j}^{\mp}$ and $\psi_{y,i,j}^{\mp}$ are calculated using the fifth-order weighted essentially non-oscillatory scheme [10]. The time integration of equation (12), as well as of the reinitialization equation, is performed using the third-order total variation diminishing Runge–Kutta scheme [20]. A first-order upwind scheme in space and forward Euler time integration are used for solving the extension field [20]. The time steps in our explicit method for time integration must satisfy the Courant–Friedrichs–Lewy condition, time step $\leq h/(\max|\text{velocity}|)$, for maintaining numerical stability, where the ‘velocity’ can be either V_{ext} , $\text{sign } q$, or $\text{sign } d_i$, depending on the equation being solved. With an anisotropic interfacial energy, we take the time-step as $\Delta t = 0.5h^4$ [4]. The details of the discretization scheme, as well as a verification against several known solutions, are given in our earlier work [1]. We note that all the partial differential equations being solved here, as part of the LSM routine, are hyperbolic in nature and hence require only suitable initial conditions (rather than boundary conditions) for their solvability [20].

The overall computational algorithm for the LSM can be summarized in the following steps [1]:

- (a) Check if ψ is a SDF. If ψ is not an SDF, then convert it to an SDF by reinitializing it in the domain of computation.
- (b) Construct two computational tubes T_1 and T_2 , surrounding the zero level set of ψ , such that $|\psi| \leq c_1$ in T_1 and $|\psi| \leq c_2$ in T_2 . We take $c_1 = 2h$ and $c_2 = 4h$. Construct a third tube, $T_3 = \{\mathbf{x} : \psi(\mathbf{x} + \boldsymbol{\delta}) < c_2, \text{ for } |\boldsymbol{\delta}| < h\}$, containing T_2 in addition to the grid points adjacent to T_2 .
- (c) Calculate V using the linear kinetic relation which requires the elasticity solution (obtained from XFEM for the existing precipitate shape) in the neighborhood of the zero level set and the geometry of the zero level set.
- (d) Compute κ and its surface Laplacian first inside T_1 and then extend it to $T_2 \setminus T_1$.
- (e) Compute V inside T_1 and then extend it to $T_2 \setminus T_1$.
- (f) Update ψ by integrating the modified Hamilton–Jacobi equation (10) inside T_2 .
- (g) Reinitialize the updated ψ inside region T_3 using the reinitialization equation.
- (h) The process is repeated with the reinitialized ψ , starting with step (a), until equilibrium is achieved.

4. Results

We will be providing the results of our simulations for four cases: isotropic elasticity with isotropic interface energy, anisotropic elasticity with isotropic interface energy, isotropic elasticity with anisotropic interface energy, and anisotropic elasticity with anisotropic interface energy. The first two cases are well documented in the literature and the corresponding results can be seen as verification of our numerical methodology. In all the cases, we assume dilatational strain, i.e. $\epsilon^* = \epsilon^* \mathbf{1}$. The anisotropy in the bulk elasticity, whenever considered, is assumed to be cubic such that the plane–strain stress–strain relationship is given by

$$\begin{pmatrix} \sigma_{11} \\ \sigma_{22} \\ \sigma_{12} \end{pmatrix} = \begin{pmatrix} C_{11} & C_{12} & 0 \\ C_{12} & C_{11} & 0 \\ 0 & 0 & C_{44} \end{pmatrix} \begin{pmatrix} \epsilon_{11} \\ \epsilon_{22} \\ \epsilon_{12} \end{pmatrix},$$

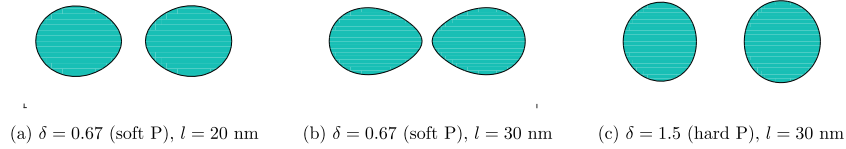
where C_{11} , C_{12} , and C_{44} are elastic constants. These three constants are related to Young’s modulus E , Poisson’s ratio ν , and shear modulus μ as $E = (C_{11}^2 + C_{11}C_{12} - 2C_{12}^2)/(C_{11} + C_{12})$, $\nu = C_{12}/(C_{11} + C_{12})$, and $\mu = C_{44}$, respectively. The anisotropic ratio $A_r = 2C_{44}/(C_{11} - C_{12})$ ($= 2\mu(1 + \nu)/E$) is used to quantify the deviation from isotropy as well as to identify the elastically soft directions: $A_r = 1$ for isotropic material (wherein $\mu = E/(2(1 + \nu))$), $A_r < 1$ for $\langle 11 \rangle$ as elastically soft direction, and $A_r > 1$ for $\langle 10 \rangle$ and $\langle 01 \rangle$ as elastically soft directions [29]. The constitutive parameters for various materials used in this paper are collected in table 1. We also introduce a dimensionless parameter

$$L = \frac{C_{44}(\epsilon^*)^2 l}{\gamma_0}, \quad \text{where } l = \sqrt{\frac{A_0}{\pi}}$$

is the equivalent radius of the precipitate (or a group of precipitates) obtained from the fixed total area A_0 of the precipitates. The parameter L captures the interplay between bulk elasticity and interface energy for a fixed size of the precipitates and given misfit strain. Whenever the bulk elasticity is taken to be isotropic, we use a dimensionless parameter $\delta = E_p/E_M$, where

Table 1. Elastic material constants and anisotropic ratio.

	C_{11} (GPa)	C_{12} (GPa)	C_{44} (GPa)	A_r
Ni [25]	246.5	147.3	127.4	2.57
Al [25]	107.3	60.9	28.3	1.22
Ni ₃ Al [7]	179	123	81	2.89
NiAl [7]	161	107	85	3.15

**Figure 4.** Equilibrium shape of two interacting precipitates with isotropic interfacial energy density and isotropic bulk elasticity.

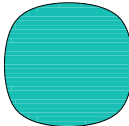

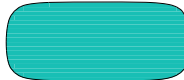
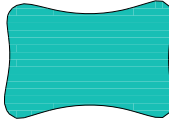
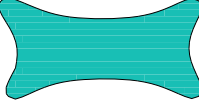




E_P and E_M denote the Young's modulus of the precipitate and the matrix, respectively; hence $\delta < 1$ for soft precipitates, $\delta > 1$ for hard precipitates, and $\delta = 1$ for an elastically homogeneous system. The domain Ω is taken to be a square of size $200 \text{ nm} \times 200 \text{ nm}$. The precipitates are located at the center of the domain with sizes that are small compare to the domain size.

The equilibrium shapes are obtained when the magnitude of decrease in the total energy reduces below a tolerance level for several iterations. It should be noted that the final configuration can be claimed to be only in a meta-stable local equilibrium state; we do not explore the possibility of achieving the global minima in the energy landscape.

4.1. Isotropic bulk energy and isotropic interface energy

With isotropic bulk energy, isotropic interface energy, and dilatational misfit strain, the equilibrium shape of a single precipitate, softer than the matrix, is circular below a critical equivalent radius and elliptical above it. The equilibrium shape is always circular if the precipitate is harder or of the same constituent as of the matrix [12]. We consider two precipitates, separated by a finite distance, at the center of a large matrix. The interfacial energy is constant such that $\gamma = \gamma_0 = 0.05 \text{ J m}^{-2}$. We take $\epsilon^* = 0.01$. Three cases are reported. Two of these correspond to having softer precipitates, with Young's modulus of the precipitate and the matrix as $E_P = 100 \text{ GPa}$ and $E_M = 150 \text{ GPa}$, respectively, first with an equivalent radius significantly below the critical value (for the corresponding single precipitate, which is 35.62 nm) and then for an equivalent radius close to the critical value. The third case corresponds to having a harder precipitate, with $E_P = 150 \text{ GPa}$ and $E_M = 100 \text{ GPa}$. In all the cases, both for the precipitates and the matrix, the Poisson's ratio $\nu = 0.33$. The results are given in figure 4. The initial configurations are two same-sized circles separated (center to center) by a distance 2.1 times the respective equivalent radius. For softer precipitates, the two precipitates are attracted to each other while developing a pointed tip in the region of interaction; the effect is more pronounced with an increasing size of the precipitates. On the other hand, when the precipitates are hard they repel and develop a lower curvature in the interaction region. These results are qualitatively in agreement with those of Jou *et al* [14].

Table 2. Equilibrium precipitate shapes with isotropic interfacial energy density and cubic bulk elasticity.

P/M	$L = 3$	$L = 7$	$L = 12$
Ni/Ni			
Al/Ni			
Ni/Al			

4.2. Anisotropic bulk energy and isotropic interface energy

We take $\gamma = \gamma_0 = 0.05 \text{ J m}^{-2}$, $\epsilon^* = 0.01$, and other material constants as given in table 1. The equilibrium shape of an isolated precipitate, with cubic bulk elasticity, isotropic interfacial energy, and dilatational misfit, depends on the relative material properties of the precipitate and the matrix. There exists a critical value of the parameter L below which the precipitate shape is dominated by the interfacial energy, and hence possesses more symmetry; beyond the critical value, the bulk elastic energy starts to dominate thereby reducing the symmetry in the equilibrium shape. The critical value is lower for a softer (with respect to the matrix) precipitate and higher for a harder precipitate [22]. These conclusions are substantiated from the results in table 2. When the material in both precipitate and matrix is identical (here Ni), the (locally) stable equilibrium shape changes to square-like (with rounded corners) from a circle (at $L = 0$, which corresponds to either $l = 0$ or, equivalently, an infinitely large γ_0) until a critical value beyond which it starts to stretch in an elastically soft direction, more so for an increasing L ; e.g., first row in table 2, recalling that the critical L for this case is 5.6 [29]. The critical value decreases when the precipitate is softer than the matrix, and there is a possibility for the appearance of concave shapes, predominantly due to the dominance of elastic energy; e.g., second row in table 2, where the critical L is below 3 and concavity increases with an increasing dominance of bulk elasticity (note that the shear modulus of Ni is almost 4.5 times larger than that of Al, see table 1) [22]. Finally, when the precipitate is harder than the matrix, e.g., third row in table 2, the critical L increases (here considerably greater than 12) and the interfacial energy strongly dominates the shape (which remains circular) [22].

We consider two precipitates, with the initial configuration as two same-sized circles separated (center to center) by a distance 2.1 times the equivalent radius. The final (locally) stable equilibrium configuration for various cases are collected in figure 5. We first consider Ni_3Al precipitates in NiAl matrix. The elastic constants of both these material are close to each other, with the former being slightly softer than the latter (the shear modulus of NiAl is 1.05 times larger than that of Ni_3Al , see table 1). We obtain two results for two widely different sizes of the precipitates, one below the critical value (for the corresponding single precipitate) and one higher than the critical value. When $L = 3$, see figure 5(a), the equilibrium shape is a

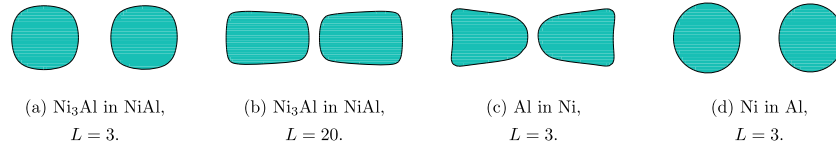


Figure 5. Equilibrium shape of two interacting precipitates of same size with isotropic interfacial energy density and cubic bulk elasticity.

pair of two square-like objects which have moved close to each other (when compared to the initial configuration). At $L = 20$, see figure 5(b), the precipitates come closer and stretch in an elastically soft direction, narrowing down slightly in the region of interaction [22, 32]. When the precipitates (Al) are considerably softer than the matrix (Ni), they demonstrate a peculiar shape, while coming close to each other, developing a nose in the region of interaction, see figure 5(c). On the other hand, when the precipitates (Ni) are considerably harder than the matrix (Al), as in figure 5(d), they tend to repel each other while getting slightly compressed along the horizontal axis, the latter due to a decrease in curvature in the region of interaction.

4.3. Isotropic bulk energy and anisotropic interface energy

We now obtain equilibrium precipitate shapes with isotropic elastic energy in the bulk and anisotropic interface energy density. The latter is considered in a form introduced in equation (4). We fix the value of certain parameters: $\gamma_0 = 0.05 \text{ J m}^{-2}$, $\alpha_e = 0.25$, $\delta_r = 0.01$, and $\epsilon^* = 0.01$. The Poisson's ratio is taken to be uniform in the domain, $\nu = 0.33$. We take $n = 4$ in the expression for interface energy density, such that the corresponding Wulff shape is a square with rounded corners.

We first consider an isolated precipitate with softer material properties, i.e. $E_P = 100 \text{ GPa}$ and $E_M = 150 \text{ GPa}$ ($\delta = 0.67$). Our aim is to develop a bifurcation curve which demonstrates a symmetry breaking transition with an increase in precipitate size. We introduce two non-dimensional parameters: the aspect ratio $X = |a - b|/(a + b)$, where a and b are maximum length dimensions of the precipitate in the horizontal and vertical directions, and $\xi = l/l_c$, where l_c is the critical equivalent radius at which bifurcation happens for the present set of parameters; $l_c = 22.15 \text{ nm}$. The resulting bifurcation plot is given in figure 6. The four-fold symmetric shape continues to be the stable shape until $\xi = 1$; the corners become less round and the edges become flatter with increasing ξ . It remains an equilibrium solution beyond this point (with even sharper facets) but is replaced by two-fold rectangle-like shapes as the stable equilibrium. Below $\xi = 1$, the interfacial energy dominates the shape but, for $\xi > 1$, elasticity starts to dominate thereby stretching the equilibrium shapes in one direction. The precipitates tend to become increasingly plate like, elongated in one direction, while maintaining facets (which develop slight convexity for large l) only in a direction orthogonal to the elongation. Also, as expected, the value of l_c decreases with increasing softness (decreasing δ) of precipitates; e.g., first two rows of table 3. We found no bifurcation for the cases when material is elastically homogeneous or when the precipitate is hard; the equilibrium precipitate shapes always maintained the four-fold symmetry, however becoming increasingly circular for higher δ , e.g., last two rows of table 3.

Next, we determine the equilibrium shape of two interacting precipitates which, in their initial configuration, are same-sized circles with a (center to center) distance equal to twice the equivalent radius. We obtain results at two equivalent length values (20 nm and 30 nm) for four cases of relative elastic moduli given in terms of δ (as in table 3). The results are presented in

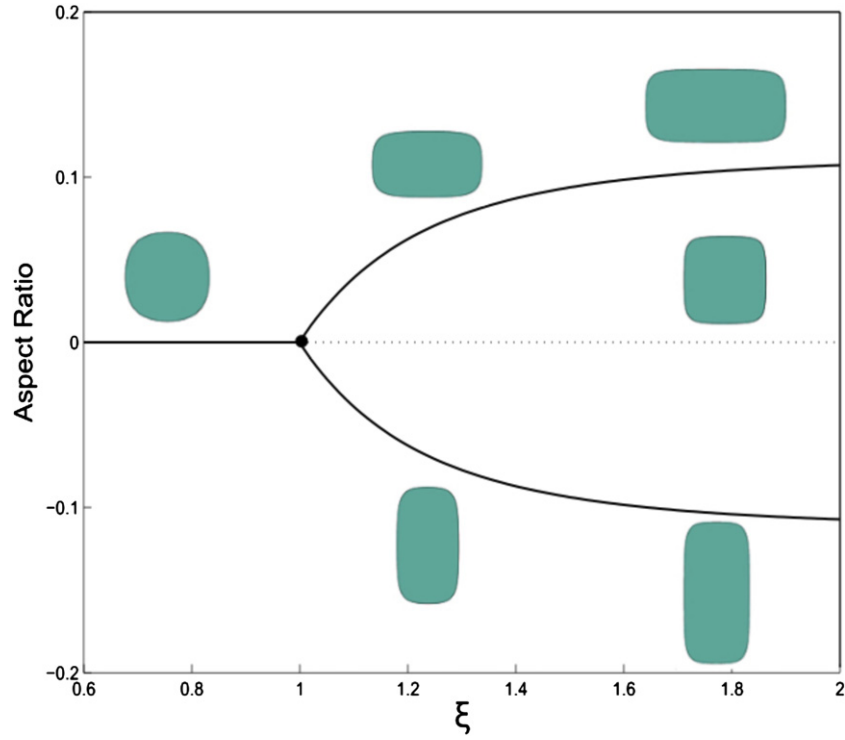


Figure 6. Bifurcation plot showing equilibrium shapes of a soft precipitate ($\delta = 0.67$) for different sizes, with anisotropic interfacial energy density and isotropic bulk elasticity.

table 4. The soft precipitates tend to be attracted to each other; they develop higher curvatures in the region of interaction, prominently so at higher equivalent lengths and increased softness (e.g., $\delta = 0.05$ and $l = 30$ nm). The hard precipitates demonstrate repulsion while deviating slightly from their four-fold shape. The inner edges of the hard precipitates are observed to become flatter with increasing l and increasing δ . The results for two different equivalent sizes demonstrate the effect of interplay between the anisotropic interfacial energy and the bulk isotropic energy, with the former dominating for the lower value of l and the latter for the higher value of l .

Continuing with our results on interacting precipitates, we consider three precipitates in a matrix. The initial configuration consists of three same-sized circles arranged in an ‘L’ shape. We consider two scenarios: one with precipitates softer than the matrix ($E_M = 250$ GPa and $E_P = 100$ GPa) and second with precipitates harder than the matrix ($E_M = 100$ GPa and $E_P = 250$ GPa), see figure 7. In the former case, the two precipitates, located at the ends, move toward the middle precipitate while elongating in a direction aligned with their axial position. A slight increase in the area of middle precipitate is also observed. In the latter case, the precipitates repel each other while retaining forms close to the Wulff shape.

4.4. Anisotropic bulk energy and anisotropic interface energy

In this section, we determine equilibrium precipitate shapes considering anisotropy in both bulk elasticity and interface energy. The former is assumed to be cubic with material parameters

Table 3. Equilibrium precipitate shape of a single precipitate with anisotropic interfacial energy density and isotropic bulk elasticity for various δ (with $E_P = 100$ GPa) and l values.

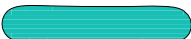


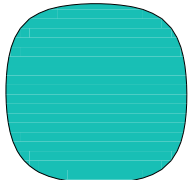
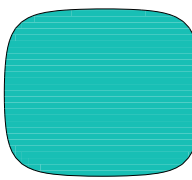
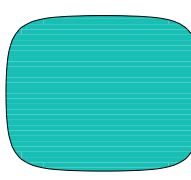
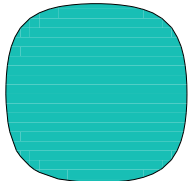
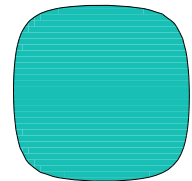
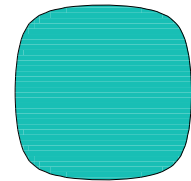
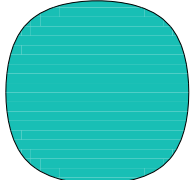
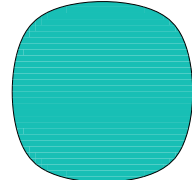
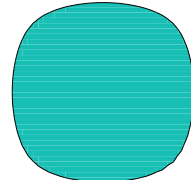
















δ	$l = 20$ nm	$l = 32$ nm	$l = 35$ nm
0.05			
0.67			
1.5			
20			

Table 4. Equilibrium shape of two interacting precipitates with anisotropic interfacial energy density and isotropic bulk elasticity for various δ (with $E_P = 100$ GPa) and l values.

δ	$l = 20$ nm		$l = 30$ nm	
0.05				
0.66				
1.5				
20				

given in table 1. The anisotropic interface energy density is of the form given in equation (4). For all the simulations in this section we fix $\gamma_0 = 0.05 \text{ J m}^{-2}$, $\delta_r = 0.01$, and $\alpha_e = 0.25$. We also fix the value of equivalent radius as $l = 30$ nm, and use variations in the dilatational misfit strain ϵ^* to vary the value of the dimensionless parameter L .

We begin by considering an elastically homogeneous medium with Ni as the material for both the precipitate and the matrix. We fix the value of interface anisotropy parameter as $n = 6$. The Wulff shape is therefore given by a hexagon with rounded corners. We evaluate

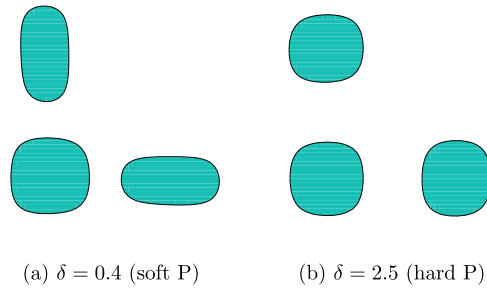


Figure 7. Equilibrium shape of three, initially circular and same-sized, precipitates ($l = 30$ nm) with anisotropic interfacial energy density and isotropic bulk elasticity.

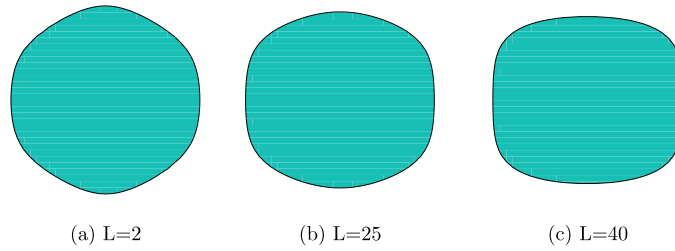
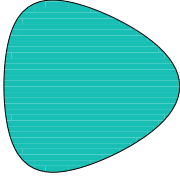
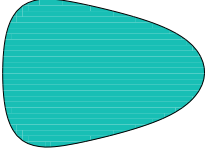
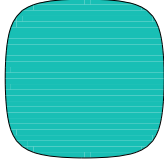

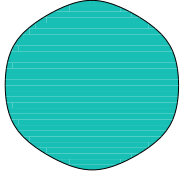
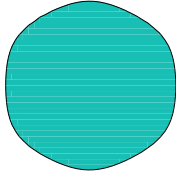


Figure 8. Equilibrium shapes for Ni precipitate in Ni matrix for different values of L keeping $n = 6$.

the equilibrium shape for three values of L , representing various degrees of interplay between the interfacial anisotropy and the elastic anisotropy (although we are varying the value of ϵ^* to vary the value of L , we can interpret the change in L in terms of variation in relative energy magnitudes). The initial shape is always taken to be an ellipse with an aspect ratio of 1.12. The results are given in figure 8. For $L = 2$, the equilibrium shape is strongly dominated by the anisotropy of interfacial energy density and therefore resembles the associated Wulff shape with six-fold symmetry. At $L = 25$, the equilibrium shape deviates from a hexagon, tending to become more rectangular, although the six faces remain discernible. The resulting shape has a lower symmetry than a hexagon. The change in symmetry can be attributed to the growing influence of elastic anisotropy at higher L . The domination of elastic anisotropy over interface anisotropy becomes unambiguous at $L = 40$ where the equilibrium precipitate shape resembles a rectangle with rounded corners. The effect of interfacial anisotropy is now absent and the final shape is clearly an outcome of the cubic elasticity with stretching along an elastically soft direction.

Continuing with the same material configuration as the preceding paragraph, we now compare the equilibrium shapes for three different values of the anisotropy parameter, $n = 3, 4$ & 6 , each with two values of L (2 and 7). The three values of n correspond to Wulff shapes in the form of a triangle, square, and hexagon, respectively, with rounded corners. The results are given in table 5. At $L = 2$, the equilibrium shape in all the cases is the corresponding Wulff shape, indicating the dominance of interfacial anisotropy at low L . At $L = 7$, a symmetry transition is observed for $n = 3$ and $n = 4$, from three-fold to one-fold for the former and from four-fold to two-fold for the latter. The stretching in shapes is along an elastically soft direction. For $n = 6$, however, the six-fold symmetry is retained even at $L = 7$. This indicates

Table 5. Equilibrium shapes for Ni precipitate in Ni matrix with variation in the degree of interface anisotropy parameter.

n	$L = 2$	$L = 7$
3		
4		
6		

an higher value of L , at the bifurcation point, for this case in comparison with the other two cases.

Next, we explore solutions for isolated inhomogeneous precipitates. The interface energy parameters are fixed as above with $n = 6$. We consider a soft precipitate of Al in a Ni matrix and hard precipitate of Ni in Al matrix. The elastic material parameters are given in table 1. The interplay between the two energies is captured by parameter L , as before. The equilibrium shapes, for $L = 7$ and 25, are collected in table 6. The corresponding solutions for the homogeneous case (Ni in Ni) are also reported in the same table for comparison. For the soft precipitate case, the six-fold hexagonal symmetry is missing at $L = 7$, unlike the other two systems, as the precipitate takes a shape tending towards a rectangle. At $L = 25$, the equilibrium shape becomes rectangular, with rounded corners and slightly concave edges. This is in contrast with the homogeneous case where the precipitates retains the Wulff shape at $L = 7$ and only begins to flatten slightly in the vertical direction at $L = 25$. It becomes more rectangular, however with convex edges, at higher L , as noted in figure 8. The hard precipitate, on the other hand, shows no deviation from the Wulff shape even for large values of L .

Finally, we obtain the equilibrium shape of two interacting precipitates. We consider three cases: homogeneous, soft, and hard precipitate, at two different values of L , analogous to the preceding paragraph. The initial configuration is taken as two circular precipitates of equal area separated (center to center) at a distance of 2.1 times the equivalent radius. The results are given in table 7. At $L = 7$, the two homogeneous precipitates take the Wulff shape while moving inwards toward each other (when compared with the initial configuration). At $L = 25$, the precipitates are further drawn to each other with a nose of higher curvature in the region of interaction. The six-fold hexagonal symmetry of the individual precipitate is now lost as they are stretched in one direction with more rounding at their edges. When the precipitates are relatively soft, as in the second row of table 7, the distance between their inner edges is less than their homogeneous counterpart and the noses are sharper and well developed [16]. When

Table 6. Equilibrium shapes for isolated homogeneous, soft, and hard precipitates with anisotropic interfacial energy density ($n = 6$) and cubic bulk elasticity.

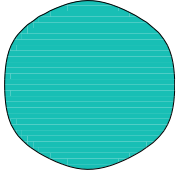
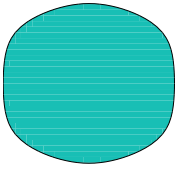
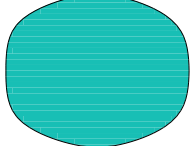

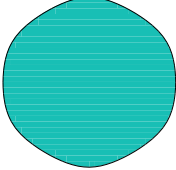
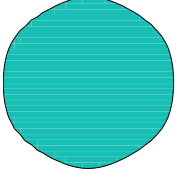












P/M	$L = 7$	$L = 25$
Ni/Ni		
Al/Ni		
Ni/Al		

Table 7. Equilibrium shapes for two homogeneous, soft, and hard precipitates with anisotropic interfacial energy density ($n = 6$) and cubic bulk elasticity.

P/M	$L = 7$		$L = 25$	
Ni/Ni				
Al/Ni				
Ni/Al				

the precipitates are hard, as in the third row of table 7, they repel each other, increasingly so at their inner edges (more prominent at higher L); the hexagonal symmetry is lost with these inner edges turning into elongated vertical facets.

5. Conclusion

We have revisited the problem of finding equilibrium shapes of single and multiple misfitting precipitates in a large matrix, possibly inhomogeneous, with dilatational misfit strains, and anisotropies in both bulk elasticity and interfacial energy density. Assuming the precipitate–matrix interface to be sharp, we developed a novel solution procedure based on a numerical formulation which couples XFEM with anisotropic LSM. The latter is complicated due to the incorporation of non-convex crystalline energies and curvature regularization. The

anisotropies have been observed to influence the shape depending on their relative magnitude and the size of the precipitate among other factors. The present work can be extended in several directions. For instance, to study the equilibrium shape of many particle system, their merger, their splitting, etc, to study the dynamics of evolving precipitate shapes, and to study the morphological development of precipitates in the neighborhood of internal/external boundaries and topological defects.

ORCID iDs

Anurag Gupta  <https://orcid.org/0000-0002-3607-0292>

References

- [1] Basak A and Gupta A 2014 A two-dimensional study of coupled grain boundary motion using the level set method *Modelling Simul. Mater. Sci. Eng.* **22** 055022
- [2] Belytschko T, Gracie R and Ventura G 2009 A review of extended/generalized finite element methods for material modeling *Modelling Simul. Mater. Sci. Eng.* **17** 043001
- [3] Bhadak B, Sankarasubramanian R and Choudhury A 1995 Phase-field modeling of equilibrium precipitate shapes under the influence of coherency stresses *Metall. Mater. Trans. A* **49** 5705–26
- [4] Chopp D L and Sethian J A 1999 Motion by intrinsic Laplacian of curvature *Interfaces Free Bound.* **1** 1–18
- [5] Di Carlo A, Gurtin M E and Podio-Guidugli P 1992 A regularized equation for anisotropic motion-by-curvature *SIAM J. Appl. Math.* **52** 1111–9
- [6] Duddu R, Bordas S, Chopp D and Moran B 2008 A combined extended finite element and level set method for biofilm growth *Int. J. Numer. Methods Eng.* **74** 848–70
- [7] Fährmann M, Hermann W, Fährmann E, Boegli A, Pollock T M and Sockel H G 1999 Determination of matrix and precipitate elastic constants in (γ - γ') Ni-base model alloys, and their relevance to rafting *Mater. Sci. Eng. A* **260** 212–21
- [8] Fried E and Gurtin M E 2004 A unified treatment of evolving interfaces accounting for small deformations and atomic transport with emphasis on grain-boundaries and epitaxy *Adv. Appl. Mech.* **40** 1–177
- [9] Ji H and Dolbow J E 2004 On strategies for enforcing interfacial constraints and evaluating jump conditions with the extended finite element method *Int. J. Numer. Methods Eng.* **61** 2508–35
- [10] Jiang G S and Peng D 2000 Weighted ENO schemes for Hamilton–Jacobi equations *SIAM J. Sci. Comput.* **21** 2126–43
- [11] Jog C S, Sankarasubramanian R and Abinandanan T A 2000 Symmetry-breaking transitions in equilibrium shapes of coherent precipitates *J. Mech. Phys. Solids* **48** 2363–89
- [12] Johnson W C and Cahn J W 1984 Elastically induced shape bifurcations of inclusions *Acta Metall.* **32** 1925–33
- [13] Joshi T 2018 Shape evolution of precipitates with anisotropic interfacial energies *Masters Thesis* Indian Institute of Technology, Kanpur
- [14] Jou H-J, Leo P H and Lowengrub J S 1997 Microstructural evolution in inhomogeneous elastic media *J. Comput. Phys.* **131** 109–48
- [15] Kolling S, Mueller R and Gross D 2003 The influence of elastic constants on the shape of an inclusion *Int. J. Solids Struct.* **40** 4399–416
- [16] Leo P H, Lowengrub J S and Nie Q 2000 Microstructural evolution in orthotropic elastic media *J. Comput. Phys.* **157** 44–88
- [17] Moës N, Cloirec M, Cartraud P and Remacle J-F 2003 A computational approach to handle complex microstructure geometries *Comput. Methods Appl. Mech. Eng.* **192** 3163–77
- [18] Moës N, Dolbow J and Belytschko T 1999 A finite element method for crack growth without remeshing *Int. J. Numer. Methods Eng.* **46** 131–50
- [19] Osher S and Sethian J A 1988 Fronts propagating with curvature-dependent speed: algorithms based on Hamilton–Jacobi formulations *J. Comput. Phys.* **79** 12–49

- [20] Peng D, Merriman B, Osher S, Zhao H and Kang M 1999 A PDE-based fast local level set method *J. Comput. Phys.* **155** 410–38
- [21] Russo G and Smereka P 2000 A remark on computing distance functions *J. Comput. Phys.* **163** 51–67
- [22] Schmidt I and Gross D 1997 The equilibrium shape of an elastically inhomogeneous inclusion *J. Mech. Phys. Solids* **45** 1521–49
- [23] Schmidt I, Mueller R and Gross D 1998 The effect of elastic inhomogeneity on equilibrium and stability of a two particle morphology *Mech. Mater.* **30** 181–96
- [24] Sethian J A 1996 *Level Set Methods: Evolving Interfaces in Geometry, Fluid Mechanics, Computer Vision, and Material Science* (Cambridge: Cambridge University Press)
- [25] Simmons G and Wang H 1971 *Single Crystal Elastic Constants and Calculated Aggregate Properties: A Handbook* (Cambridge, MA: MIT Press)
- [26] Smereka P 2003 Semi-implicit level set methods for curvature and surface diffusion motion *J. Sci. Comput.* **19** 439–56
- [27] Su C H and Voorhees P W 1996 The dynamics of precipitate evolution in elastically stressed solids—I. Inverse coarsening *Acta Mater.* **44** 1987–99
- [28] Su C H and Voorhees P W 1996 The dynamics of precipitate evolution in elastically stressed solids—II. Particle alignment *Acta Mater.* **44** 2001–16
- [29] Thompson M E, Su C S and Voorhees P W 1994 The equilibrium shape of a misfitting precipitate *Acta Metall. Mater.* **42** 2107–22
- [30] van der Vorst H A 1992 Bi-CGSTAB: a fast and smoothly converging variant of Bi-CG for the solution of nonsymmetric linear systems *SIAM J. Sci. Stat. Comput.* **13** 631–44
- [31] Wang Y and Khachaturyan A G 1995 Shape instability during precipitate growth in coherent solids *Acta Metall. Mater.* **43** 1837–57
- [32] Zhao X, Duddu R, Bordas S P A and Qu J 2013 Effects of elastic strain energy and interfacial stress on the equilibrium morphology of misfit particles in heterogeneous solids *J. Mech. Phys. Solids* **61** 1433–45